Draft version October 4, 2021
Typeset using LaTeX default style in AASTeX63

Constraining the relationship between surface rotation period and radial differential rotation rate in stars using asteroseismology in preparation for PLATO

Srijan Bharati Das [1], Yoshiki Hatta [2,3] and Hannah Schunker [4]

[1] Department of Geosciences
Princeton University
Princeton, New Jersey, USA
[2] Department of Astronomical Science
School of Physical Sciences
SOKENDAI, 2-21-1 Osawa, Mitaka, Tokyo 181-8588, Japan
[3] National Astronomical Observatory of Japan
2-21-1 Osawa, Mitaka, Tokyo 181-8588, Japan
[4] School of Information and Physical Sciences
University of Newcastle
Callaghan, New South Wales, Australia

ABSTRACT

The interior rotation profile for stars is poorly constrained, but is an important quantity to understand angular momentum transport in stars and stellar dynamos. Kitchatinov & Rüdiger (1999) models show that radial and latitudinal differential rotation is a function of bulk rotation rate. The upcoming PLATO mission will make asteroseismic observations of 320,743 stars offering a tantalising opportunity to understand the relationship between observed surface rotation and differential rotation for ensembles of stars. In this study we use ensemble asteroseismology to determine the future possibility of constraining the relationship between latitudinally averaged surface rotation and radial differential rotation of main sequence stars modelled by Kitchatinov & Rüdiger (1999) using observations from PLATO. We estimate the uncertainties achievable on radial differential rotation by considering the expected lower noise-level in PLATO observations. To find the number of stars expected in an ensemble we use proportionality estimates from catalogues with prior measurements of stellar surface rotation rates. We develop a two-dimensional functional fit for an ensemble of stars that can be constrained by surface rotation measurements. We find that in order to sufficiently constrain the uncertainties in the inverted rotation profiles with PLATO, we will need ensembles of the order of 10^4 stars.

Keywords: Asteroseismology — Rotation, Stellar Physics — Differential Rotation

1. INTRODUCTION

Internal rotation in stars critically governs stellar magnetism and stellar evolution. The angular velocity of rotation changes across radius as well as latitude inside a star, giving rise to differential rotation. This induces velocity shear which when coupled with magnetic fields drives the stellar dynamo (see Spruit 2002; Brun & Browning 2017; Karak et al. 2020, and references therein). The observed stellar activity cycles, on the order of tens of years, are a direct consequence of this. Stellar evolution occurring on the timescale of millions of years depend on the distribution and transport of angular momentum with differential rotation being one of its major carriers (Mestel 1953; Zahn 2008; Aerts et al. 2019). Consequently, a better understanding of stellar differential rotation would enable a more robust explanation of observed stellar activity and more accurate prediction of stellar evolution.

Corresponding author: Srijan Bharati Das
sbdas@princeton.edu

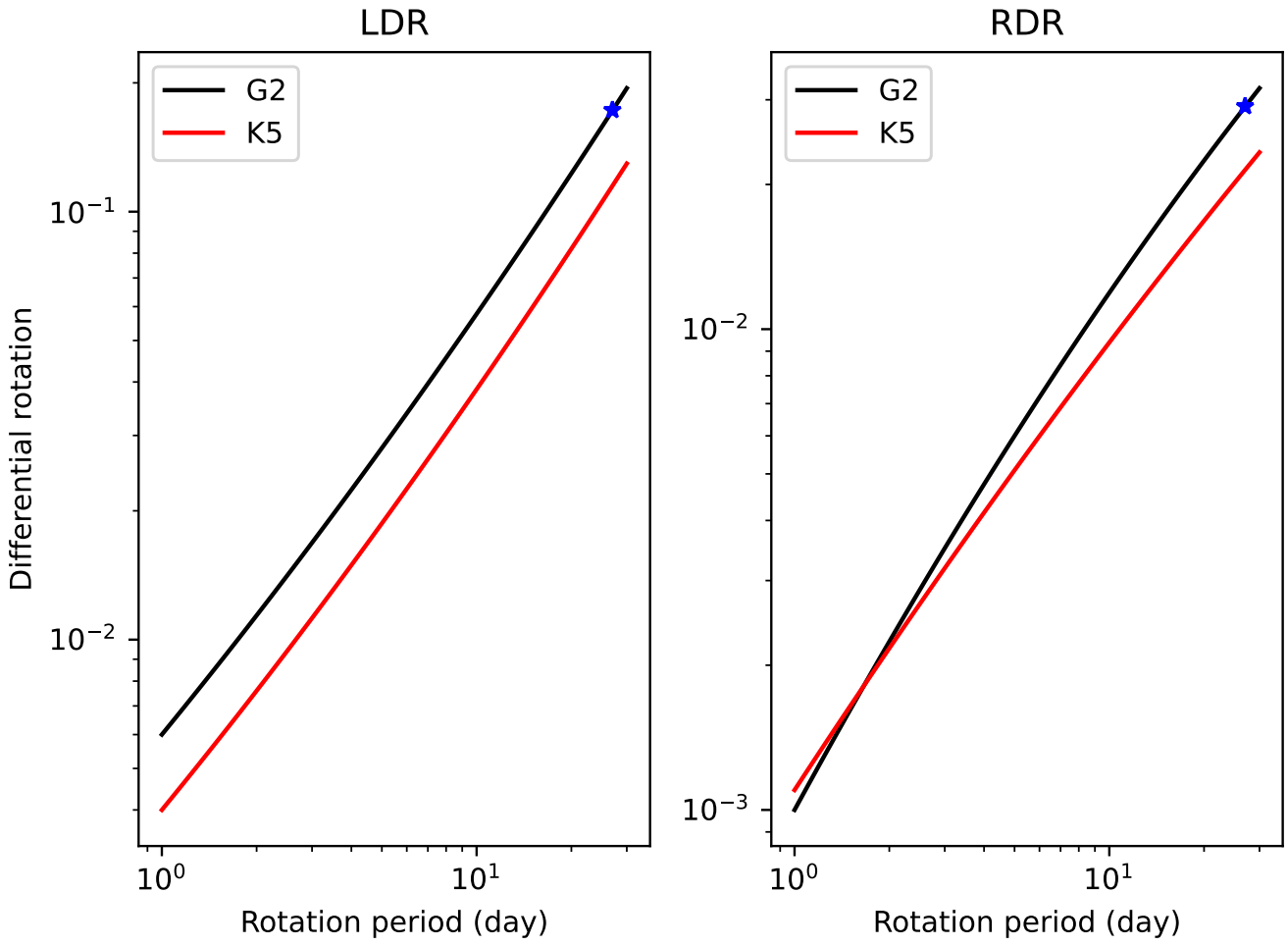

Figure 1. The radial differential rotation (RDR as in Eqn. [1]) and the latitudinal differential rotation (LDR as in Eqn. [2]) as proposed in Figure 1 in Kitchatinov & Rüdiger (1999). The *black* and *red* lines in both figures represent G2 and K5 stars respectively. These power laws are used to construct the synthetic differential rotation profile $\Omega(r, \theta)$ as outlined in Appendix B. The blue star of the G2 power-law denotes the Sun.

Differential rotation in the Sun has been extensively studied over the last few decades using precise helioseismic measurements (see Howe 2008, and references therein). The poles rotate slower than the equator with an average surface rotation period of 27 days. A shallow fast rotating layer, in radius, lies at about $0.95R_\odot$ while the radiative interior and the core rotate approximately as a solid body. Latitudinally averaged solar rotation profile shows a jump near the solar tachocline at $0.7R_\odot$. This leads us to believe in the presence of similar shear layers in radius for other Sun-like stars as well. In this study, we have assumed the simplest approximation to this radial profile using a step-function in radius (see Section 4.1). This is similar to the assumption made in Schunker et al. (2016), with the exception that we account for latitudinal differential rotation as well.

Evolution of stellar rotation is notoriously difficult to model self-consistently (Potter et al. 2012). Kitchatinov & Rüdiger (1999) (hereafter KR99) simulated a model for global circulation based on the mean-field hydrodynamics of rotating turbulent fluids (Ruediger 1989). A series of differential rotation models with $P_{\rm rot}$ ranging from a day to a little over the solar rotation period were applied to the main-sequence spectral classes G2 and K5. From their numerical results, they found that rotation follows power-laws for variation of relative differential rotation $(\Delta\Omega)/\Omega$ as a function of rotation rate Ω. They defined Radial Differential Rotation (RDR) which quantifies the radial variation of the latitudinally averaged differential rotation and the Latitudinal Differential Rotation (LDR) which quantifies the

latitudinal variation of rotation at the stellar surface:

$$\text{RDR}: \quad \left(\frac{\Delta\Omega}{\Omega}\right)_{\text{rad}} = \frac{\bar{\Omega}_{\text{bot}} - \Omega_0}{\Omega_0} \quad , \tag{1}$$

$$\text{LDR}: \quad \left(\frac{\Delta\Omega}{\Omega}\right)_{\text{lat}} = \frac{\Omega_{\text{equator}} - \Omega_{\text{pole}}}{\Omega_0} \quad , \tag{2}$$

where, $\bar{\Omega}_{\text{bot}}$ and Ω_0 are the latitudinally averaged angular velocity at the bottom of the convection zone and at the surface, respectively. Ω_{equator} is the surface angular velocity at the equator and Ω_{pole} is the surface angular velocity at the pole. Figure 1 shows the power-laws for RDR and LDR suggested in KR99. Observational verification of these relations would constrain the models of KR99. As seen in Figure 1, to do so, we need (A) the surface rotation rate Ω_0 which is readily measured using multiple techniques, and (B) the asteroseismic inversions for differential rotation (LDR and RDR) which is the focus of our study.

Asteroseismology has historically provided the most precise measurements of stellar parameters such as age, radius, mass, density (as in the recent study by Bellinger et al. 2019) and rotation (Nielsen et al. 2017; Suto et al. 2019). Analyzing the photometric observations of the stellar brightness reveals peaks in the frequency domain corresponding to the eigenmodes of oscillation. These eigenmodes are labelled by n, ℓ, m where n represents the radial order (number of nodes along radius), ℓ the angular degree (total number of nodal great circles on the sphere) and the azimuthal order m (number of zero crossings going once around the equator). Asteroseismic studies use the differences in location between observed and expected frequency peaks of these global eigenmodes of pulsation to infer stellar internal properties. In the presence of rotation (or any other spherically asymmetric perturbation) individual peaks corresponding to unperturbed multiplets split into multiple peaks depending on the azimuthal order m. The width of these peaks depend on mode damping (inversely related to the mode lifetime). If the stellar rotation is not fast enough, the mode frequencies are not split sufficiently to resolve each widened peak separately. These widened peaks, when split, appear merged or "broadened" rather than split. These frequency splittings can be measured using well-developed, sophisticated fitting techniques (see Gizon et al. 2013).

Earlier studies on LDR were based on non-asteroseismic method such as (A) fourier analysis of the spectroscopic line profiles, (B) tracking of surface magnetic features as they travel across latitudes, and (C) photometric variability induced due to sunspots distributed across latitudes. With fabulous new photometric and spectro-polarimetric observations being available from recent and upcoming space-based missions, interior of stars beyond the Sun are now accessible using asteroseismology. Benomar et al. (2018) reported the LDR for 13 sun-like stars based on independent asteroseismic inversion for each star using Kepler observations. As seen in their Figure 1, the inferred error-bars are significantly large compared to the scale necessary to constrain RDR and LDR in KR99. Consequently, with the currently available temporal length of photometric observations, inversions using independent asteroseismic studies performed on a single-star, lack the precision to verify the consistency of observations with the numerically predicted power-laws in KR99. This does not rule out the viability of independent asteroseismology as and when future missions with much longer observation times and the possibility of using doppler velocity measurements become available.

Constraining internal rotation for sub-giant stars with observable mixed-modes (p and g) is feasible using single-star measurements (e.g. Deheuvels et al. 2012). This is much more challenging for sun-like main-sequence stars where only p-modes are observable (Nielsen et al. 2014). Schunker et al. (2016) carried out numerical investigations demonstrating that inversions for a "common" parameter — in their case the RDR — using a group or "ensemble" of stars yield significantly smaller uncertainties of this parameter as compared to independent asteroseismology. This method is called ensemble asteroseismology. They showed that the estimated errors from ensemble asteroseismology are lower by a factor of $\sqrt{N_{\text{stars}}}$ as compared to independent asteroseismology.

The Kepler mission (Borucki et al. 2010; Koch et al. 2010) provided a wealth of asteroseismic observations from a large number of stars with observational times stretching over months to years. Chaplin et al. (2014) used data from Kepler to infer fundamental properties of over 500 stars with solar-like oscillations. Currently, Kepler provides the best quality of data for performing asteroseismic analysis on rotational splitting to infer stellar internal rotation. The possibility of forming large ensembles depends on the number of stars observed and the quality of measurements obtained from space-based missions. PLAnetary Transits and Oscillations of stars (PLATO), currently planned to be launched in 2026, is a space-based mission being developed by the European Space Agency (ESA). It will observe approximately 50,000 stars for extended periods of 2-3 years with the same and shorter cadence as Kepler (60 seconds) for some of the best quality asteroseismic measurements. Therefore, we expect unprecedented observations of light

curves from an enormous number of stars with half the noise as Kepler. This makes PLATO a promising mission for implementing ensemble asteroseismology.

PLATO will be observing a large number of stars in the main-sequence (F, G, K). The primary target of this study is to inspect if the accuracy of the asteroseismic ensemble inversions for differential rotation is sufficient to constrain the power-laws of LDR and RDR as predicted in KR99. Larger number of stars in an ensemble implies smaller error-bars (which scales as $1/\sqrt{N_{\rm stars}}$). Small enough error-bars would enable us to test the power laws of LDR and RDR in KR99.

1.1. *The PLATO Input Catalogue*

The PLATO Input Catalogue (PIC) (Montalto et al. 2021) contains 320,743 PLATO targets in the long-duration fields. For validating the KR1999 models, the specific PLATO targets we are interested in are main-sequence F, G, K type stars with sampling times sufficient to measure solar-like oscillations. The PLATO P1 sample of 15,094 stars has a sampling time of 25 seconds and from the 272,617 fainter (and thus noisier) stars in the P5 sample, 9000 stars will be observed with a sampling time of 25 seconds and at least 10% will be observed with a 50 second sampling time.

Each of the North and South long-duration fields will be observed for up to three years (Montalto et al. 2021). The North field incorporates the Kepler field which is centred at RA 19h22m40s (J2000) and DEC 44°30′00". Kepler observed stars 183-920 parsecs away (600-3000 ly) and PLATO observes stars a little closer at 146-428 parsecs away.

2. MODELLING STELLAR ROTATION

PLATO has a planned launch scheduled no earlier than 2026. In this study we carry out inversions on synthetic frequency splitting measurements expected to be observed by PLATO. This involves (A) using previous catalogues to estimate the expected number of stars in PIC to estimate the expected number of stars in each ensemble (see Section 3), and, (B) generating artificial noise with the knowledge of expected ppm/hour from PLATO (see Section 2.2). As a first step towards modeling the axisymmetric differential rotation profile $\Omega(r,\theta)$, we choose to parameterize it in angular degree s as follows.

$$\Omega(r,\theta) = \sum_s \Omega_s(r)\,\frac{{\rm d}P_s(\cos\theta)}{{\rm d}\cos\theta} = -\sum_s \frac{\Omega_s(r)}{\sin\theta}\,\frac{{\rm d}P_s(\cos\theta)}{{\rm d}\theta} \quad . \tag{3}$$

The inversion is then carried out for the coefficients $\Omega_s(r)$. It is important to note that (A) since differential rotation $\Omega(r,\theta)$ is symmetric about the equator, s is odd, and, (B) from selection rules imposed by the inversion kernel (as seen later in Eqn. [6]) $s_{\rm max} = 3$. This is because of the triangle inequality $0 \le s \le 2\ell$ imposed by the Wigner 3-j symbol $\begin{pmatrix} s & \ell & \ell \\ 0 & 1 & -1 \end{pmatrix}$ and $\ell = 2$ being the largest reliably resolved angular degree to be used from observations.

We choose $\Omega_s(r)$ to be in the form of a step-function. Unlike helioseismology where modes upto $\ell = 1000$ can be reliably observed, asteroseismology restricts us to $\ell \le 3$. $\ell = 0$ does not carry information about rotational splitting. So, for each radial order n we can use only $\ell = 1, 2$. But the number of radial orders observed is numbered in the tens located around the multiplet (n,ℓ) with the peak frequency $\omega_{\rm max}$. This results in the dataset for observed rotational splitting being limited to a small number of modes. which consequently reduces the number of constraints and hence hinders a detailed radial inversion. So, we contrain the quantity of interest — $\Delta\Omega_s$. So, $\Omega_s(r)$ for each angular degree s is expressed either in terms of the parameters $(\Omega_s^{\rm in}, \Omega_s^{\rm out})$ or $(\Omega_s^{\rm out}, \Delta\Omega_s)$. Here, $\Delta\Omega_s = \Omega_s^{\rm in} - \Omega_s^{\rm out}$. In our study, we choose the latter convention. See Figure 2 for a visual representation of this simple model and the labelled associated parameters.

We use the predicted power-law from Figure 1 in KR99 to construct the synthetic differential rotation profile. Figure 1 shows the LDR($P_{\rm rot}$) and RDR($P_{\rm rot}$) as suggested in KR99. This gives us the parameters $P_{\rm rot}$, $\left.\frac{\Delta\Omega}{\Omega}\right|_{\rm rad}$ and $\left.\frac{\Delta\Omega}{\Omega}\right|_{\rm lat}$. Appendix B details how these parameters are used to generate the model parameters $\Omega_1^{\rm out}, \Delta\Omega_1$ and $\Omega_3^{\rm out}$. These are used to generate $\Omega_s(r)$ which is then used in obtaining the synthetic frequency splittings $\delta\omega_{nlm}$ according to Eqn. (5). This gives us a noise-free estimate of the $\delta\omega_{nlm}$ measurements to be used in inversions.

2.1. *Frequency splitting due to differential rotation*

Flow due to differential rotation $\mathbf{v}_{\rm rot}(r,\theta) = \mathbf{r} \times \mathbf{\Omega}(r,\theta)$ is an axisymmetric (zonal) toroidal flow. A common way (see Ritzwoller & Lavely 1991; Schou et al. 1998; Vorontsov 2011) to parameterize differential rotation $\mathbf{\Omega}(r,\theta)$ is to

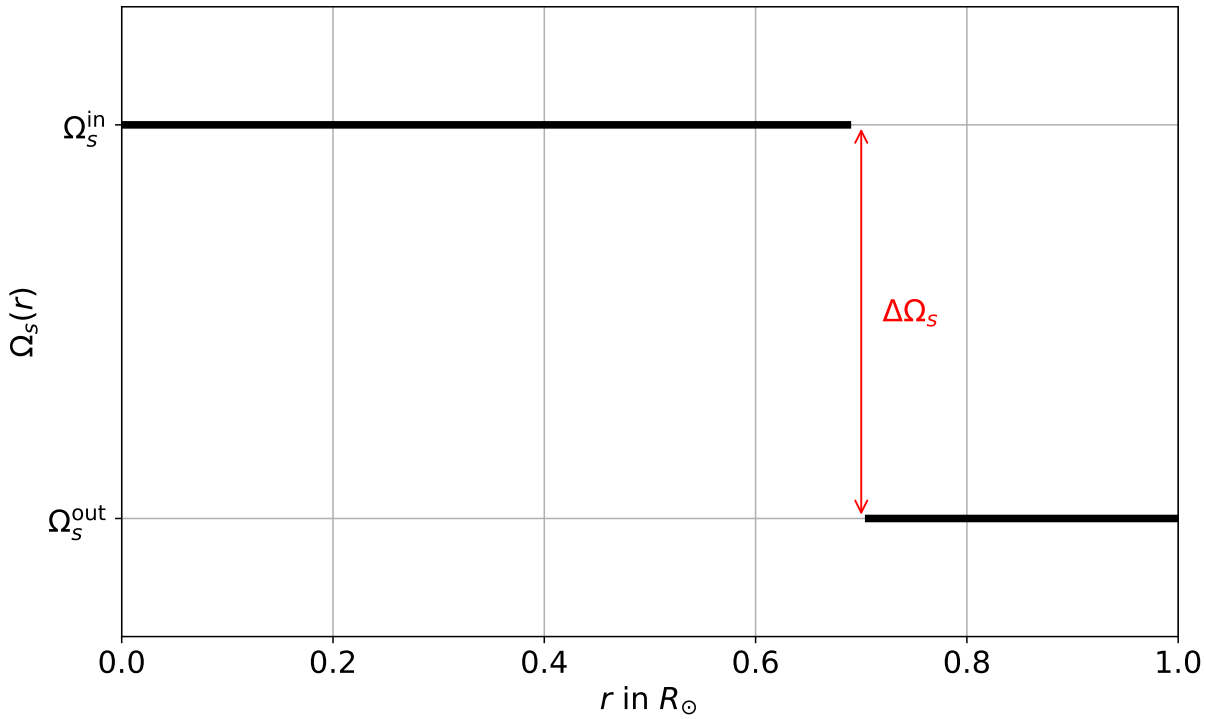

Figure 2. Representative plot showing the step function used in functional fitting of $\Omega_s(r)$ as detailed in Section 4.1, more specifically Eqn. (11). An averaged internal rotation (for $r \leq r_{\rm cz}$) and an averaged external rotation (for $r > r_{\rm cz}$) is denoted by $\Omega_s^{\rm in}$ and $\Omega_s^{\rm out}$, respectively. The jump in rotation rate is defined by $\Delta\Omega_s = (\Omega_s^{\rm in} - \Omega_s^{\rm out})$. So, the radial variation of $\Omega_s(r)$ can be parameterized either as $(\Omega_s^{\rm in}, \Omega_s^{\rm out})$ or as $(\Omega_s^{\rm out}, \Delta\Omega_s)$. In this study we choose the latter set of parameters. For this representative plot, $r_{\rm cz}$ is denotes the base of the solar convection zone at $0.7R_\odot$.

decompose it in the basis of legendre polynomials P_s as in Eqn. (3). Using these basis coefficients $\Omega_s(r)$, we can similarly parameterize $\mathbf{v}_{\rm rot}(r,\theta)$ as

$$\mathbf{v}_{\rm rot}(\theta,\phi) = -\sum_s r\,\Omega_s(r)\left(\frac{4\pi}{2s+1}\right)^{1/2}\partial_\theta Y_{s0}(\theta,\phi)\,\hat{e}_\phi \tag{4}$$

where, Y_{st} are spherical harmonics (following the convention in Edmonds 1960), $\hat{e}_\phi$ is the unit vector along the ϕ axis and s is the angular degree of differential rotation. Note that the azimuthal order is zero for axisymmetric perturbations. From linear perturbation theory, it can be shown that the eigenfrequencies of the background stellar model due to an axisymmetric flow perturbation of the form $\delta\mathcal{L} = -2i\rho_0\mathbf{v}_{\rm rot}\cdot\boldsymbol{\nabla}$ induces frequency shifts (or splittings)

$$\delta\omega_{n\ell m} = \sum_{s=1,3,\ldots}\int_{r=0}^{R_*}\Omega_s(r)\,\mathcal{K}^s_{nlm}(r)\,{\rm d}r, \tag{5}$$

where the sensitivity kernel $\mathcal{K}^s_{nlm}(r)$ for $\Omega_s(r)$ can be expressed as (see Appendix A in Vorontsov 2011),

$$\begin{aligned}\mathcal{K}^s_{n\ell m}(r) = (-1)^{m+1}\ell\,(\ell+1)\,(2\ell+1)\begin{pmatrix} s & \ell & \ell \\ 0 & 1 & -1\end{pmatrix}\begin{pmatrix} s & \ell & \ell \\ 0 & m & -m\end{pmatrix}\rho_0\,r^2 \\ \times\left[U^2 - 2\,U\,V + \left(\ell(\ell+1) - \frac{1}{2}s(s+1)\right)V^2\right] \quad .\end{aligned} \tag{6}$$

Here, r is the grid along radius, $U = U_{nlm}(r), V = V_{nlm}(r)$ are the radial and the horizontal eigenfunctions, ρ_0 is the density profile of the stellar model obtain from `MESA`. It must be noted that the Wigner 3-j symbols impose selection

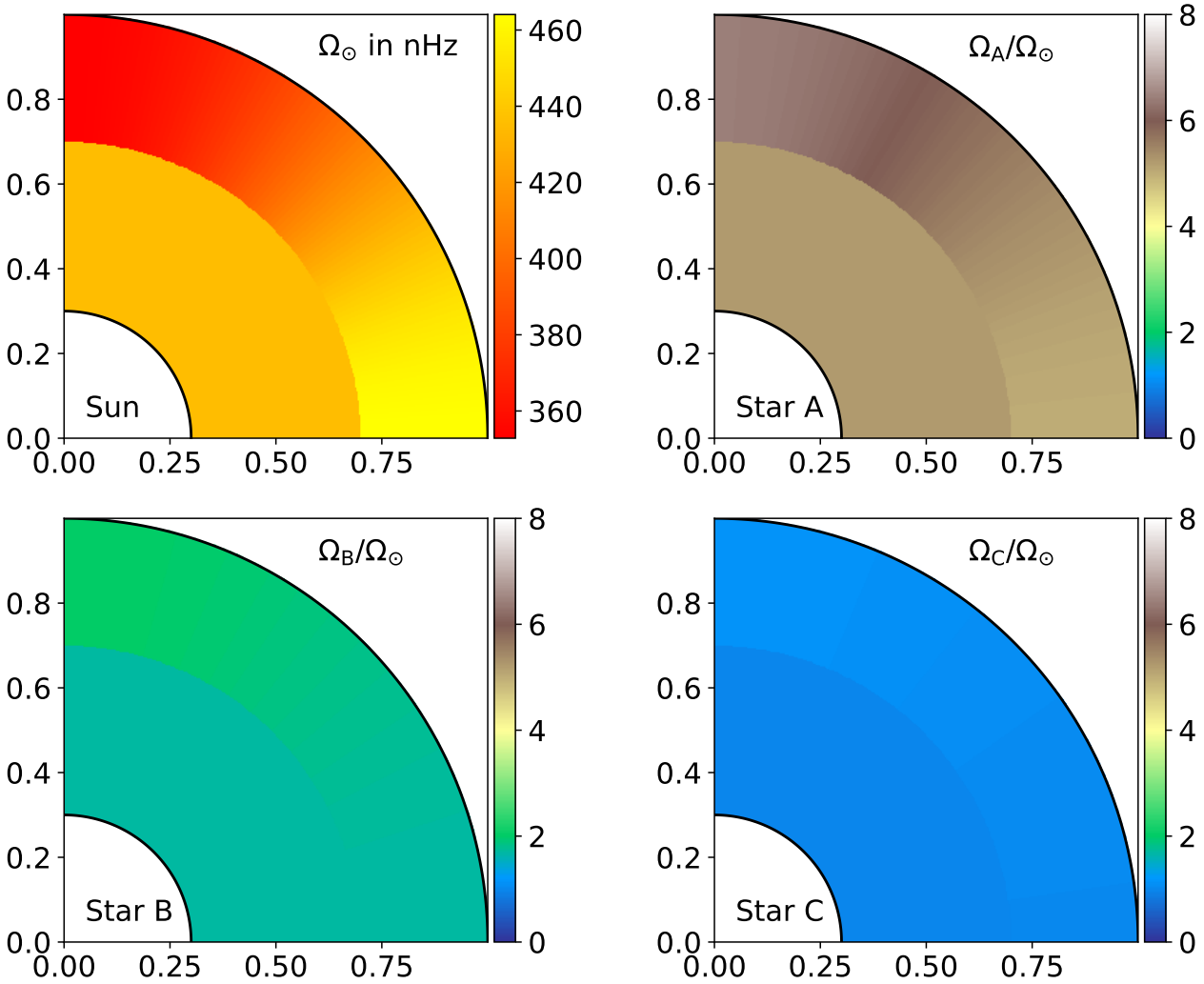

Figure 3. 2D quadrants of the Sun and three hypothetical stars (Star A, Star B and Star C) when modeled in (r, θ) as an axisymmetric flow which is a step-function in r (as in Figure 2) with maximum angular degree $s_{\max} = 3$. The *top-left* panel shows differential rotation in the Sun $\Omega_\odot(r, \theta)$ as found in the 1.5D inversion in Schou et al. (1998) — plotted here after approximating $\Omega_s(r)$ as a step-function in radius. The remaining three panels show the "point-wise" relative differential rotation $\Omega_*(r, \theta)/\Omega_\odot(r, \theta)$. We choose the average surface rotation periods (in days) $P^{\rm A}_{\rm rot} = 5, P^{\rm B}_{\rm rot} = 15$ and $P^{\rm C}_{\rm rot} = 25$. This is the same as the average of the windows W1, W2 and W3 plotted on the x-axis in Figure 5.

rules that allow non-vanishing values for $\mathcal{K}^s_{nlm}$ for odd s. This implies that given the observed frequency splitting values $\delta\omega_{nlm}$, Eqn. (5) allows inverting for only equatorially symmetric $\mathbf{\Omega}(r, \theta)$.

2.2. *Modelling uncertainties on the splittings*

The uncertainty in inverted parameters depend critically on the uncertainty in measurements. Therefore, to generate realistic synthetic observations, we need a noise model to account for the observational errors and to develop a robust algorithm for inversions. We use the noise model from Libbrecht (1992) for the uncertainty in the observed frequency splitting $\sigma(\delta\omega_{nlm})$,

$$\sigma(\omega_{n\ell m}) = f(\beta)\,\frac{\Gamma_{n\ell m}}{4\pi T} \quad . \tag{7}$$

Here, Γ_{nlm} is the mode linewidth and T is the total temporal length of observation. $f(\beta) = (1+\beta)^{1/2}\left[(1+\beta)^{1/2} + \beta^{1/2}\right]^3$ and $\beta = \mathcal{B}_{nlm}/H_{nlm}$ where, $\mathcal{B}_{nlm}$ is the background noise at ω_{nlm} and H_{nlm} is the mode

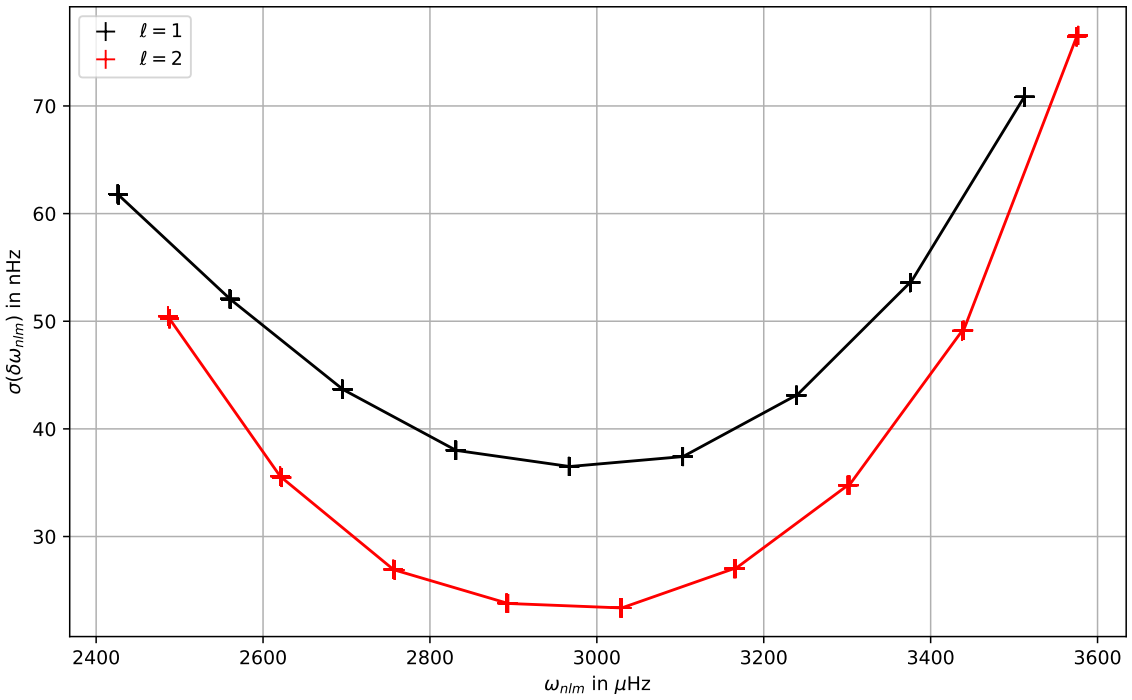

Figure 4. Variation of uncertainty in frequency splitting $\sigma(\delta\omega_{nlm})$ as a function of mode frequency ω_{nlm}. The *black* and *red* lines denote different radial orders n for angular degrees $\ell = 1$ and $\ell = 2$ respectively. Solar values are used for the linewidth Γ_{nlm}, central frequency of envelope ω_0, envelope widths σ_1 and σ_2 . These values can be found in Stahn (2010).

height in the frequency power spectrum. Details of constructing the synthetic $\mathcal{B}_{nlm}$ using the Harvey model (Harvey 1985) can be found in Stahn (2010). The mode height of a mode with frequency ω_{nlm} is given by

$$H_{nlm} = \frac{\mathcal{A}_\ell^2}{\pi\Gamma_{nlm}} F(\omega_{nlm}, \omega_0, \sigma_1, \sigma_2) \tag{8}$$

$$\text{where,} \qquad F(\omega, \omega_0, \sigma_1, \sigma_2) = \begin{cases} \left[1 + \left(\frac{\omega-\omega_0}{2\pi\sigma_1}\right)^2\right]^{-2} & \omega \le \omega_0 \\ \left[1 + \left(\frac{\omega-\omega_0}{2\pi\sigma_2}\right)^2\right]^{-2} & \omega > \omega_0 \end{cases} \tag{9}$$

where, $\mathcal{A}_\ell$ is the maximum of the envelope of modes with angular degree ℓ, $F(\omega_{nlm}, \omega_0, \sigma_1, \sigma_2)$ given by Eqn. (9) is the envelope function centered at frequency ω_0 with σ_1 and σ_2 being the widths of the envelope below and above ω_0. We scale the parameters from solar values determined by Stahn (2010) using the following scaling laws (see Chaplin et al. 2009; Schunker et al. 2016):

$$\frac{\Gamma_{nlm,*}}{\Gamma_{nlm,\odot}} = \frac{T_{\mathrm{eff},*}^4}{T_{\mathrm{eff},\odot}^4}, \qquad \frac{H_{nlm,*}}{H_{nlm,\odot}} = \frac{g_\odot^2}{g_*^2}, \qquad \frac{\mathcal{B}_{nlm,*}}{\mathcal{B}_{nlm,\odot}} = \frac{\nu_{\max,*}}{\nu_{\max,\odot}}, \tag{10}$$

where, subscripts $\odot$ and $*$ refer to Sun and other stars respectively.

As in Schunker et al. (2016), we construct the uncertainty in frequency splittings $\sigma(\delta\omega_{nlm})$ using $\sigma(\delta\omega_{nlm}) = \sigma(\omega_{nlm})/m$. Figure 4 shows the variation of $\sigma(\delta\omega_{nlm})$ as a function of mode frequency ω_{nlm} for the Sun.

We use *Kepler* observations as a quantitative measure of the noise (in ppm/hour) to be used to generate synthetic frequency splitting data. The stars in the P1 sample will be measured at a noise level of 50 ppm/hour which is half of the noise level in Kepler measurements. The P5 sample of at least 36,271 fainter stars will have a Kepler-like noise level of 100 ppm/hour.

3. DEFINING STELLAR ENSEMBLES

The goal of this study is to estimate uncertainties associated to radial differential rotation (RDR) and latitudinal differential rotation (LDR) via ensemble asteroseismology using PLATO. The uncertainties scale as $1/\sqrt{N_*}$ where N_* is the number of stars in an ensemble. Therefore, we need to have an estimate of the number of stars we should expect in each PLATO ensemble.

McQuillan et al. (2014) measured the rotation periods of 34,030 (25.6%) of the 133,030 main-sequence Kepler targets. Hotter stars tend to be faster rotators, and faster rotators are easier to measure rotation periods for. Therefore, of the 34,030 detected rotation periods there are about

- 52% with $0 < P_{\rm rot} < 10$: Equivalent to 22085 stars in PLATO. We label this window of time-period as W1.
- 30% with $10 < P_{\rm rot} < 20$: Equivalent to 12894 stars in PLATO. We label this window of time-period as W2.
- 12% with $20 < P_{\rm rot} < 30$: Equivalent to 5132 stars in PLATO. We label this window of time-period as W3.
- 6% with $P_{\rm rot} > 30$: Equivalent to 2344 stars in PLATO.

4. INVERSE PROBLEM: THEORY AND NOTATIONS

4.1. *Functional Fitting*

In this section, we discuss the details of the "functional fitting" method deriving inspiration from Section 3.3 in Schunker et al. (2016); Kawaler et al. (1999) (hereafter K99). Frequency splittings in a star can be reliably observed upto an angular degree $\ell \leq 3$ (although, in this study we consider an upper limit of $\ell \leq 2$) for a few tens of radial orders n. Such limited information (as compared to helioseismology), compels us to assume simple functional forms for $\Omega_s(r)$. In this paper, we choose to project $\Omega_s(r)$ onto a step function. We choose functional fitting over the more traditional Regularized Least Square (RLS) method since K99 show (Section 4 therein) that if the actual rotation rate does not conform to the regularization, RLS inversions "yield markedly unrealistic results". In the next subsections, we assume a discretized radial grid r_j where $j \in [0, M]$ such that $r_0 = 0$ and $r_M = R_*$. A function in $r = r_j$ can be expressed as a sum over basis polynomials $F_k(r_j)$ which are appropriated weighted a_k,

$$\Omega_s(r_j) \;=\; \Omega^s_j \;=\; a^s_k\, F_k(r_j) = F_{jk}\, a^s_k \quad , \tag{11}$$

where we have used Einstein's summation convention over repeated indices (used in the rest of the paper unless mentioned otherwise).

4.1.1. *1D inversion: Radial profile only*

This is the simplest case and is just meant to be a rephrasing of K99 in terms of our problem parameters. The frequency splittings can be expressed as

$$\delta\omega_{n\ell m} = \int_{r=0}^{R_*} \Omega(r)\, \mathcal{K}_{nlm}(r)\, {\rm d}r, \tag{12}$$

Adhering to the same convention as in K99, we shall denote the multiplet (n, ℓ, m) using the label i where $i \in [1, N]$. So, Eqn. (12) can be written in the 'concise index form' $\delta\omega_i = \mathcal{K}_{ij}\, \Omega_j$. Since in our problem, the observable modes are far smaller than the ideal grid in radius we would want, we restrict ourselves to a pre-chosen functional form. This, in our case, is the following step-function in radius:

$$\Omega(r) = \begin{cases} \Omega_1^{\rm out} + \Delta\Omega_1 & r < r_{\rm cz} \\ \Omega_1^{\rm out} & r \geq r_{\rm cz} \end{cases} \tag{13}$$

For the step-function in Eqn. (13), this would imply

$$\Omega_j = (\Omega_1^{\rm out} + \Delta\Omega_1)\, F_{j1} + \Omega_1^{\rm out}\, F_{j2} \quad , \tag{14}$$

where $F_{j1} = H(r_j - r_{\rm cz})$ and $F_{j2} = H(r_{\rm cz} - r_j)$ and $H(x)$ is the heaviside step function. So, comparing Eqn. (14) with Eqn. (11), we see that $a_1 = \Omega_1^{\rm out} + \Delta\Omega_1$ and $a_2 = \Omega_1^{\rm out}$. Now, the above basis functions are true if we want to invert

for $\Omega_1^{\rm in}$ and $\Omega_1^{\rm out}$. However, for our problem, we shall be inferring $\Omega_1^{\rm out}$ and $\Delta\Omega_1$. We arrive at a convenient choice for our basis functions as follows after some trivial algebra.

$$\begin{aligned}\Omega_j = (\Omega_1^{\rm out} + \Delta\Omega_1)\, H(r_j - r_{\rm cz}) + \Omega_1^{\rm out}\, H(r_{\rm cz} - r_j) &= \Omega_1^{\rm out}\, [H(r_j - r_{\rm cz}) + H(r_{\rm cz} - r_j)] \,+\, \Delta\Omega_1\, H(r_j - r_{\rm cz}) \\ &= \Omega_1^{\rm out} \,+\, \Delta\Omega_1\, H(r_j - r_{\rm cz}) \quad .\end{aligned} \tag{15}$$

So, comparing with Eqn. (11), we see if we choose $a_1 = \Omega_1^{\rm out}$ and $a_2 = \Delta\Omega_1$ then $F_{j1} = 1$ and $F_{j2} = H(r_j - r_{\rm cz})$. The final target is to extract a_k using the data $\delta\omega_i$, the analytical closed-form expressions of the kernels $\mathcal{K}_{ij}$ and basis functions F_{jk}. In 1D (where $s = 1$), using Eqn. (12) in its concise index form along with Eqn. (11), we get

$$\delta\omega_i = \mathcal{K}_{ij}\, \Omega_j \tag{16}$$

$$= \mathcal{K}_{ij}\, F_{jk}\, a_k = B_{ik}\, a_k \tag{17}$$

where we have written $B_{ik} = \mathcal{K}_{ij}\, F_{jk}$. Now, if the uncertainties in measurements of $\delta\omega_i$ are σ_i, let us define $\delta\tilde{\omega}_i = \delta\omega_i/\sigma_i$ and $A_{ik} = B_{ik}/\sigma_i$ (note, no summation over repeated indices used here). Eqn. (17) can then be written as $\delta\tilde{\omega}_i = A_{ik}\, a_k$. The elements of the data vector is populated with the frequency splittings, $d_i = \delta\tilde{\omega}_i$. Writing this in matrix form we get, $\mathsf{d} = \mathsf{A} \cdot \mathsf{a}$. Assuming A is not necessarily a square matrix, we can solve for a by taking a generalized inverse.

$$\mathsf{a} = (\mathsf{A}^T \cdot \mathsf{A})^{-1}\, \mathsf{A}^T \cdot \mathsf{d} \tag{18}$$

In the following subsections we have additional features that: (A) allow $s = 1, 3$ (2D inversions), and, (B) impose surface rotation constraints (constrained inversions). It may be important to note that the equations for these inverse problems will have the same mathematical form as Eqn. (18) with modifications to the expressions of A matrix and d vector.

4.1.2. *Adding a regularization term in 1D*

For noise-free data $\delta\omega_i$, Eqn. (16) can be derived from the minimization of the loss function χ^2 expressed as

$$\chi^2 = \sum_i \left(\delta\omega_i - \mathcal{K}_{ij}\, \Omega_j\right)^2 \tag{19}$$

with respect to the model parameter Ω_j. However, the forward model is expected to change if we add a regularization term to the minimization function. For our problem, we shall be using surface rotation $\Omega^{\rm out\,obs}$ as constraints. Including uncertainty in frequency splitting measurements $\sigma(\delta\omega_i) = \sigma_i$ and surface rotation constraint $\Omega^{\rm out\,obs}$ changes the loss function as below.

$$\begin{aligned}\chi^2 &= \sum_i \left(\frac{\delta\omega_i - \mathcal{K}_{ij}\, \Omega_j}{\sigma_i}\right)^2 + \mu \left(\Omega^{\rm out} - \Omega^{\rm out,obs}\right)^2 \quad , \\ \chi^2 &= \sum_i \left(\delta\tilde{\omega}_i - \tilde{\mathcal{K}}_{ij}\, \Omega_j\right)^2 + \mu \left(\Omega^{\rm out} - \Omega^{\rm out,obs}\right)^2 \quad ,\end{aligned} \tag{20}$$

where the $\delta\tilde{\omega}_i = \delta\omega_i/\sigma_i$ and $\tilde{\mathcal{K}}_{ij} = \mathcal{K}_{ij}/\sigma_i$. Any observational uncertainty in $\Omega^{\rm out,obs}$ is absorbed into the regularizing parameter μ. Now, if there are M radial grid points, then $\Omega^{\rm out} = \Omega_M$ (although in our case $M = 2$ effectively). So, minimizing w.r.t Ω_k gives us

$$\frac{\partial\chi^2}{\partial\Omega_k} = \left(\delta\tilde{\omega}_i - \tilde{\mathcal{K}}_{ij}\, \Omega_j\right)\left(-\tilde{\mathcal{K}}_{ik}\right) + \mu \left(\Omega_M - \Omega^{\rm out,obs}\right) \delta_{Mk} = 0 \tag{21}$$

After a few lines of algebra, this can be re-expressed as

$$\left(\tilde{\mathcal{K}}_{ik}\, \tilde{\mathcal{K}}_{ij} + \mu\, \delta_{Mk}\, \delta_{Mj}\right)\, \Omega_j = \delta\tilde{\omega}_i\, \tilde{\mathcal{K}}_{ik} + \mu\, \Omega^{\rm out,obs}\, \delta_{Mk} \tag{22}$$

Next, we use the functional fitting for $\Omega_j = F_{jk'}\, a_{k'}$ and get

$$\begin{aligned}&\mathsf{A}_{\rm reg} \,\cdot\, \mathsf{a} = \mathsf{d}_{\rm reg} \\ \text{where,}\quad &(\mathsf{A}_{\rm reg})_{kk'} = \left(\tilde{\mathcal{K}}_{ik}\, \tilde{\mathcal{K}}_{ij} + \mu\, \delta_{Mk}\, \delta_{Mj}\right)\, F_{jk'} \\ \text{and,}\quad &(\mathsf{d}_{\rm reg})_k = \left(\delta\tilde{\omega}_i\, \tilde{\mathcal{K}}_{ik} + \mu\, \Omega^{\rm out,obs}\, \delta_{Mk}\right)\end{aligned} \tag{23}$$

Finally, as mentioned before, this has the same form as Eqn. (18) with modified matrices due to regularization

$$\mathsf{a} = \left(\mathsf{A}_{\rm reg}^T \cdot \mathsf{A}_{\rm reg}\right)^{-1} \mathsf{A}_{\rm reg}^T \cdot \mathsf{d}_{\rm reg} \tag{24}$$

4.1.3. *2D inversions: Slight modification to the 1D case*

If we want to invert for the solid body component along θ given by $s = 1$ as well as the first equatorially symmetric harmonic degree given by $s = 3$. The corresponding radially discretized expression for frequency splitting $\delta\omega_{nlm}$ and functional fitting $\Omega_s(r)$ using condensed labels is given by

$$\begin{aligned} \delta\omega_i &= \Omega_j^s \, \mathcal{K}_{ij}^s \quad , \\ \Omega_j^s &= F_{jk} \, a_k^s \quad . \end{aligned} \tag{25}$$

Note that the basis polynomials F_{jk} do not inherit the angular degree s since we assume that the discontinuity exists at the same location in radius $r = r_{\rm cz}$ for both Ω_j^1 and Ω_j^3. The coefficients a_k^s are

$$\begin{aligned} a_1^1 &= \Omega^{\rm out} & a_2^1 &= \Delta\Omega^1 \\ a_1^3 &= 0 & a_2^3 &= \Delta\Omega^3 \end{aligned} \tag{26}$$

To maintain the form of Eqn. (17), the definitions of B_{ik} and a_k would be slightly altered. Since a_k is a vector of unknown parameters, we shall append the extra elements of a_k^3 under the elements of a_k^1. This would imply an extension in the number of columns of B_{ik} such that the B_{ik}^1 would form the first set of columns and B_{ik}^3 constitutes the second set of columns.

$$\begin{pmatrix} \vdots \\ \delta\omega_i \\ \vdots \end{pmatrix} = \left(\begin{array}{ccc|ccc} \ddots & \vdots & & \ddots & \vdots & \\ \cdots & B_{ik}^1 & \cdots & \cdots & B_{ik}^3 & \cdots \\ & \vdots & \ddots & & \vdots & \ddots \end{array}\right) \begin{pmatrix} \vdots \\ a_k^1 \\ \vdots \\ a_k^3 \\ \vdots \end{pmatrix} \tag{27}$$

The remaining steps stay the same with this modified form of B and a matrices. The inverse problem with appropriately modified expressions for A and a has the same form as Eqn. (18).

4.1.4. *Regularization in 2D with surface "average" rotation constraint*

In this section we shall derive the statement for the inverse problem for 2D inversions with constraint on the "average" observed surface rotation profile (see Eqn. [B3] for the averaging convention used). As shown Eqn. (B13) in Appendix B, this average observed surface rotation rate $\Omega^{\rm out,obs} = \Omega_1^{\rm out}$. Using Eqn. (11), the loss function can be written as

$$\chi^2 = \sum_i \left(\frac{\delta\omega_i - B_{ij}^s \, a_j^s}{\sigma_i}\right)^2 + \mu \left(\frac{\Omega_1^{\rm out} - \Omega^{\rm out,obs}}{\Delta\Omega^{\rm out,obs}}\right)^2 \tag{28}$$

Note that here, $B_{ij}^s = \mathcal{K}_{ik}^s \, F_{jk}$. Also, as before, we define $\delta\omega_i/\sigma_i = \tilde{\sigma}_i$, $B_{ij}^s/\sigma_i = A_{ij}^s$ and $\mu/\Delta\Omega^{\rm outobs} = \tilde{\mu}$. This gives us

$$\chi^2 = \sum_i \left(\delta\tilde{\omega}_i - A_{ij}^s \, a_j^s\right)^2 + \tilde{\mu} \left(\Omega_1^{\rm out} - \Omega^{\rm out,obs}\right)^2 \tag{29}$$

Minimizing with respect to the rotation profile $a_p^{s'}$,

$$\frac{\partial\chi^2}{\partial a_p^{s'}} = (\delta\tilde{\omega}_i - A_{ij}^s a_j^s)(-A_{ip}^{s'}) + \tilde{\mu}(\Omega_1^{\rm out} - \Omega^{\rm out,obs}) \left(\frac{\partial\Omega_1^{\rm out}}{\partial a_p^{s'}}\right) \tag{30}$$

Now, since $\Omega_1^{\rm out} = a_2^1$, so $\left(\partial\Omega_1^{\rm out}/\partial a_p^{s'}\right) = \delta^{s',1} \, \delta_{p,2}$. So, Eqn. (3) becomes

$$\frac{\partial\chi^2}{\partial\Omega_p^{s'}} = (\delta\tilde{\omega}_i - A_{ij}^s a_j^s)(-A_{ip}^{s'}) + \tilde{\mu}(a_j^s \, \delta^{s,1} \, \delta_{j,2} - \Omega^{\rm out,obs}) \, \delta^{s',1} \, \delta_{p,2} = 0 \tag{31}$$

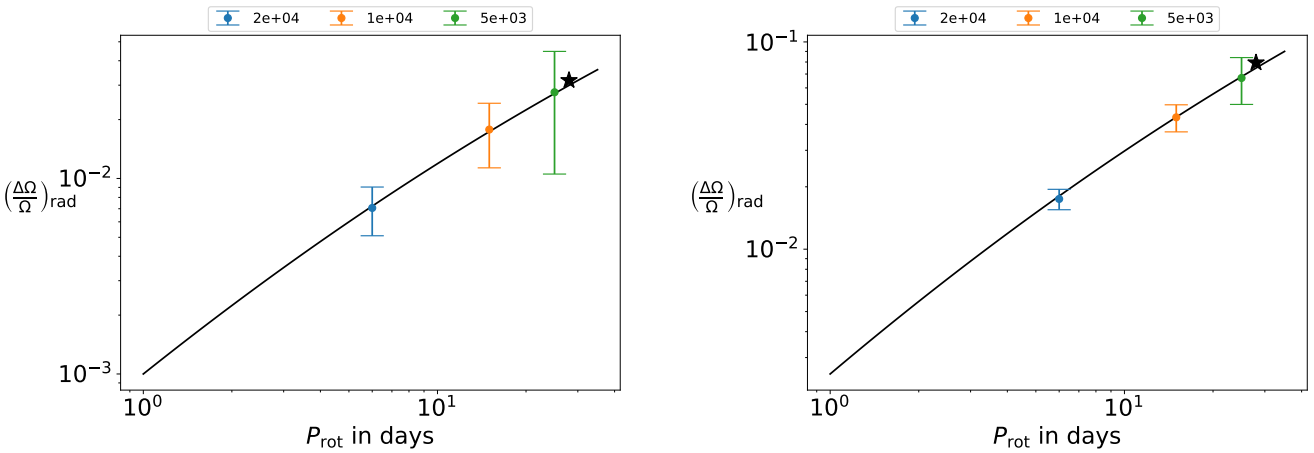

Figure 5. RDR for G2 stars scaled by a factor of 2 (*left* panel) and 5 (*right* panel) compared to Figure 1 in Kitchatinov & Rüdiger (1999) superposed with predicted error-bars from ensemble asteroseismology using "expected" PLATO measurements. The color-coded legend shows the number of stars considered in each ensemble. Ensembles are defined using frequency windows W1, W2 and W3 as defined in Section 3. The common ensemble parameter $\Delta\Omega$ is inverted for each window (W1, W2, W3) and plotted against the average $P_{\rm rot}$ of the respective window (5 days, 15 days, 25 days). The *black* star symbol denotes the Sun on this plot.

After a few lines of calculation we get

$$\left(A^{s'}_{ip}\, A^{s}_{ij}\, a^{s}_{j} + \tilde{\mu}\, \delta^{s',1}\, \delta_{p,2}\, \delta^{s,1}\, \delta_{j,2}\, a^{s}_{j}\right) = \delta\tilde{\omega}_i\, A^{s'}_{ip} + \tilde{\mu}\, \Omega^{\rm out,obs}\, \delta^{s,1}\, \delta_{p,2} \tag{32}$$

In our code, we combine the `Nparams` dimension with the `s` dimension, let us define a combined dimension for $(p\times s') = \alpha$ and $(j \times s) = \beta$. This essentially represents "flattening" the dimensions j and s to make it a single enhanced dimension of length $p \times s$. This makes the previous equation look like

$$(A_{i\alpha}\, A_{i\beta} + \tilde{\mu}\, J_\alpha\, J_\beta)\; a_\beta = \delta\tilde{\omega}_i\, A_{i\alpha} + \tilde{\mu}\, \Omega^{\rm out,obs}\, J_\alpha \tag{33}$$

where $J_\alpha = \delta^{s',1}\, \delta_{p,2}$ and $J_\beta = \delta^{s,1}\, \delta_{j,2}$ with the dimensions flattened adequately. So, we regain the usual notation

$$\mathsf{A}^{\rm 2D}_{\rm reg} \cdot \mathsf{a} = \mathsf{d}^{\rm 2D}_{\rm reg} \qquad , \tag{34}$$

where,

$$\begin{aligned} \left(\mathsf{A}^{\rm 2D}_{\rm reg}\right)_{\alpha\beta} &= A_{i\alpha}\, A_{i\beta} + \tilde{\mu}\, J_\alpha\, J_\beta \\ \left(\mathsf{d}^{\rm 2D}_{\rm reg}\right)_{\alpha} &= \delta\tilde{\omega}_i\, A_{i\alpha} + \tilde{\mu}\, \Omega^{\rm out,obs}\, J_\alpha \qquad . \end{aligned} \tag{35}$$

Again, the inverse problem Eqn. (34) for the constrained 2D case has the same form as Eqn. (18) with modified expressions for A and d.

5. CONSTRAINING RADIAL DIFFERENTIAL ROTATION AS A FUNCTION OF ROTATION

In this section, we present the results of estimating the error-bars from the frequency splitting measurements expected to be measured by PLATO. As detailed in Sections 2 and Appendix B, we construct the synthetic rotation profile for stars across rotation period $P_{\rm rot} \in [1, 30]$ using the power law given in KR99. To emulate the noise expected from PLATO measurements, we use the treatment outlined in Section 2.2. Next, we form ensembles based on windows in rotation period W1-W3 as defined in Section 3. Ensemble asteroseismology is based on forming groups with common parameters shared by stars in that ensemble. From Figure 1 we notice that the RDR increases monotonically across $P_{\rm rot}$ in log-scale. Multiplying RDR by Ω (which decreases monotonically for increasing $P_{\rm rot}$), we find that $\Delta\Omega$ remains nearly constant. This allows us to consider $\Delta\Omega$ as an ensemble parameter based on windows W1: $P_{\rm rot} \in [1, 10]$ days,

W2: $P_{\rm rot} \in [10, 20]$ days and W3: $P_{\rm rot} \in [20, 30]$ days. Again, as mentioned in Section 3, the number of stars considered in each window is inspired from cross-matching PIC with the stars in McQuillan et al. (2014) derived from the Kepler catalogue.

The RDR power-law suggested by KR99 is obtained from simulations which considers only the outer convection zone and not the radiative interior. This could lead to possible underestimation of $\Delta\Omega$. In Figure 5, we present the estimated error-bars after scaling the RDR suggested in KR99 by a factor of 2 and 5. Since the y-axes are in logarithmic scale, the size of error bars drop significantly upon such scaling. As a result, we see that the case where $\Delta\Omega$ is scaled by 5 is very tightly constrained. However, even if we scale up by a factor of 2, we find that the error bars for W1 and W2 are small enough to verify the power law. The inversions are carried out using Eqn. (18) implemented in `enseisro` (can be found in the link here).

6. DISCUSSION AND CONCLUSION

In the course of the KSPA summer program spanning six weeks, we designed the software to carry out 1D and 2D unconstrained inversions for stars using ensembles with common $\Delta\Omega$ among the stars. The primary goal of this study is to estimate error-bars of $\left(\frac{\Delta\Omega}{\Omega}\right)_{\rm rad}$ using synthetically generated expected PLATO data. From the results discussed in Section 5, we find that if KR99 had underestimated $\Delta\Omega$ by a factor of 2 or more, then the expected error-bars are sufficiently small to gauge the accuracy of their interface dynamo theory.

The immediate next steps in this study are listed below.

1. Impose surface rotation constrain based on previous independent studies using Kepler data (such as McQuillan et al. 2014). This involves modifying the expressions in the inverse problem as in Eqn. (23)-(24) and Eqn. (34)-(35).

2. Estimating error-bars for the LDR similar to that done for RDR in Figure 5. It is expected that the error bars for the LDR would be much smaller because of the significantly larger value of LDR as compared to RDR plotted in log-scale.

3. All the results presented until now was for G2 type stars. We plan to use `MESA-GYRE` to generate the stellar models for K5 type stars and subsequently their eigenfunctions and eigenfrequencies. This would allow us to generate error-bars for the K5 power-law.

The authors thank the Kavli Foundation for organizing the Kavli Summer Program In Astrophysics 2021 which facilitated this collaborative project. The authors are grateful to Dr Robert Cameron of Max Plank Institute for Solar System Research (MPS) for insightful discussions during the course of the summer program.

APPENDIX

A. TESTING THE ASYMPTOTIC APPROXIMATION

A common approximation when inferring stellar internal profiles from frequency splitting measurements is to use the semiclassical approximation for Wigner 3-j symbols (Brussaard & Tolhoek 1957; Dahlen & Tromp 1998). We see from Eqn. (6), that these Wigner 3-j symbols appear in the exact expressions for rotation kernels (as well as kernels for any other perturbation). For modes with high ℓ such that $s << \ell$, a Wigner 3-j symbol can be approximated by associated Legendre polynomials as

$$\text{Approximation 1}: \qquad \begin{pmatrix} s & \ell & \ell \\ 0 & m & -m \end{pmatrix} \simeq \frac{(-1)^{\ell+m}}{(2\ell)^{1/2}} P_s^0\left(\frac{m}{\ell}\right) \qquad , \tag{A1}$$

and the product of Wigner 3-j symbols as in Eqn. (6) is approximated under similar asymptotic limit as

$$\text{Approximation 2}: \qquad \begin{pmatrix} s & \ell & \ell \\ 0 & 1 & -1 \end{pmatrix} \begin{pmatrix} s & \ell & \ell \\ 0 & m & -m \end{pmatrix} \simeq (-1)^{\frac{s-\ell'+\ell+2m+1}{2}} \frac{(s+\ell'-\ell)!!(s-\ell'+\ell)!!}{2\ell^2(s+\ell'-\ell)!} P_s^{\ell'-\ell}\left(\frac{m}{\ell}\right). \tag{A2}$$

It is to be noted that the above asymptotic limit holds for odd s only. We tested the goodness of this approximation with $s = 3$, which is the largest angular degree of differential rotation we are currently interested in this study.

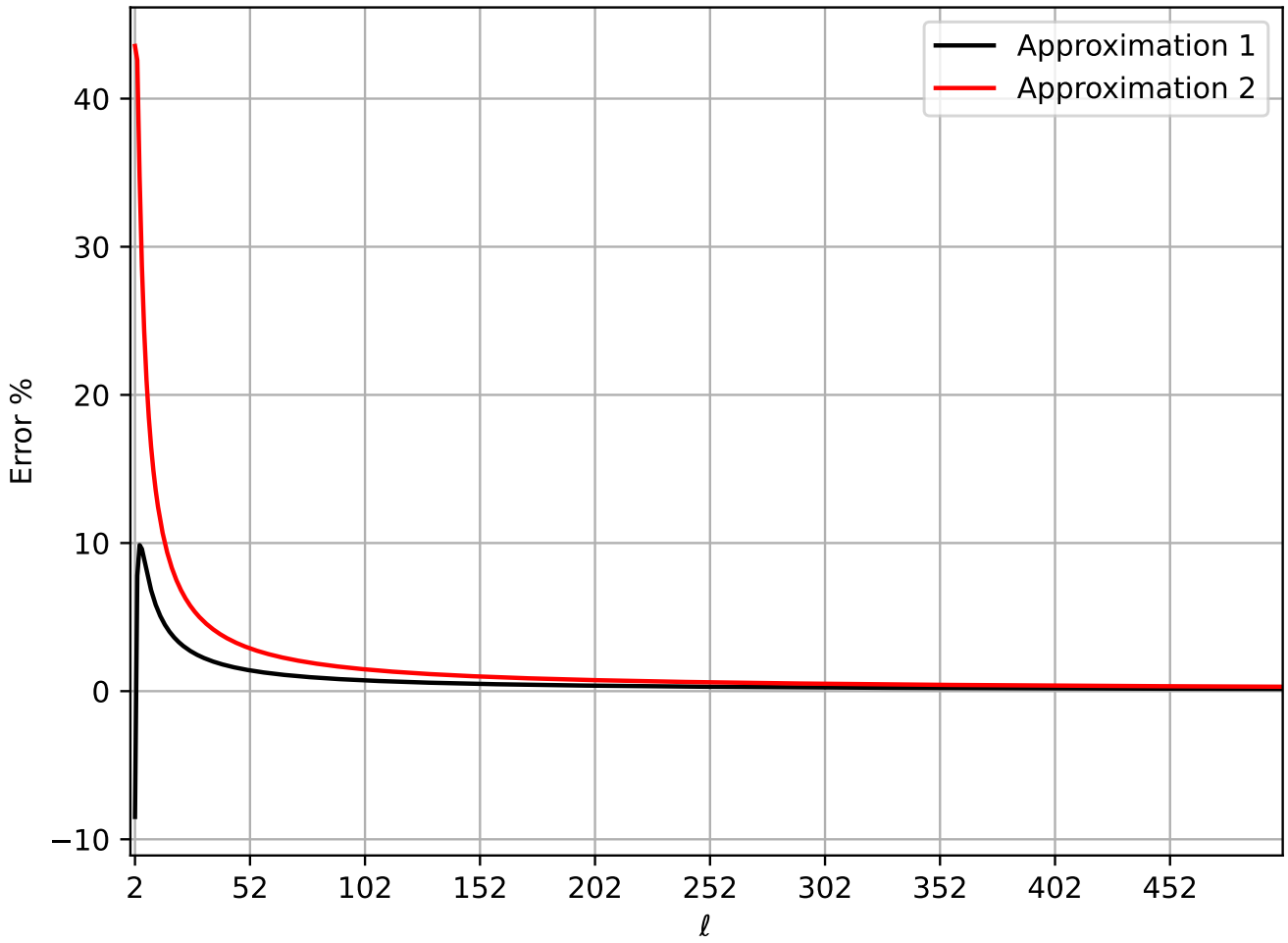

Figure 6. Percentage error in semi-classical asymptotic approximation of the Wigner 3-j symbols. The *black* line shows the error in percent when using the Approximation 1 as given by Eqn. (A1) and the *red* line shows the error in percent when using Approximation 2 as given by Eqn. (A2). It is to be noted that other studies in asteroseismology often use the Approximation 2 in the rotation kernel given by Eqn (6).

Varying the angular degree of the mode over wide range $\ell \in [1, 500]$, demonstrates that for $\ell \lesssim 14$ the error in such approximations exceed 10%. Figure 6 shows the percentage error in approximations given by Eqn. (A1) in *black* and Eqn. (A2) in *red*. In this study and the software developed `enseisro`, we strictly stick to the exact expressions using Wigner 3-j symbols.

B. GENERATING SYNTHETIC ROTATIONAL PROFILES FROM KR99

In this section, we would like to artificially generate rotational profiles (for Sun-like stars) which follow the trend found in Figure 1 of KR99. In particular, we are looking for a relation between the expressions in KR99 and those in our parameterization as in Sections 4.1.1, 4.1.2, 4.1.3 and 4.1.4.

First, we present some definitions seen in KR99. Ω_0 is the latitudinally averaged rotation rate of the surface, namely,

$$\Omega_0 = \frac{3}{4}\int_0^\pi \Omega(R,\theta)\sin^3\theta\,\mathrm{d}\theta, \tag{B3}$$

where the weighting $\sin^3\theta$ is included so that Ω_0 is unchanged even if the angular momentum is latitudinally re-distributed (see the text in KR99). The stellar radius is given as R. $\Omega_0 = 2\pi/P_{\rm rot}$, where $P_{\rm rot}$ is the rotational period.

Following the same latitudinal averaging as Eqn. (B3) at the base of the convection zone, $\bar{\Omega}_{\rm bot}$ is defined as below

$$\bar{\Omega}_{\rm bot} = \frac{3}{4}\int_0^\pi \Omega(r_{\rm cz},\theta)\sin^3\theta\,{\rm d}\theta, \tag{B4}$$

where $r_{\rm cz}$ is the radial location of the base of the convection zone.

KR99 defines two important parameters that describe the differential rotation of the star. One is the surface latitudinal differential rotation (LDR),

$$\frac{\Delta\Omega}{\Omega_0} \equiv \frac{\Omega_{\rm equator}-\Omega_{\rm pole}}{\Omega_0}, \tag{B5}$$

and the other is the latitudinally averaged rotation inhomogeneity with depth (the radial differential rotation, or RDR),

$$\left.\frac{\Delta\Omega}{\Omega_0}\right|_{\rm rad} \equiv \frac{\bar{\Omega}_{\rm bot}-\Omega_0}{\Omega_0}. \tag{B6}$$

In Figure 1 of KR1999, the horizontal axis is $P_{\rm rot}$, and the vertical axes are $\frac{\Delta\Omega}{\Omega_0}$ and $\left.\frac{\Delta\Omega}{\Omega_0}\right|_{\rm rad}$ for the left and right panels in Figure 1, respectively. The starting point is our way of parameterization of the internal rotation,

$$\Omega(r,\theta) = \sum_s \Omega_s(r)\,\frac{{\rm d}P_s(\cos\theta)}{{\rm d}\cos\theta}. \tag{B7}$$

Since we are considering the case with $s = 1, 3$, we can express $\Omega(r,\theta)$ more explicitly as below:

$$\Omega(r,\theta) = \Omega_1(r) + \Omega_3(r)\left(\frac{15}{2}\cos^2\theta - \frac{3}{2}\right), \tag{B8}$$

where the Legendre polynomials with degrees one and three have been substituted. By assuming step-like functions for $\Omega_1(r)$ and $\Omega_3(r)$, we have the following expression:

$$\Omega(r,\theta) = \Omega_1^{\rm in}F_{\rm in} + \Omega_1^{\rm out}F_{\rm out} + \Omega_3^{\rm out}F_{\rm out}\left(\frac{15}{2}\cos^2\theta - \frac{3}{2}\right), \tag{B9}$$

where, step-like functions for the radiative region and the convective envelope are expressed by $F_{\rm in}$ and $F_{\rm out}$, respectively. Note that $\Omega_1^{\rm in}$, $\Omega_1^{\rm out}$, and $\Omega_3^{\rm out}$ are constants here. We also assume that the radiative region is not latitudinally differentially rotating, i.e. $\Omega_3^{\rm in} = 0$.

The rest of the Appendix details the process of generating artificial rotational profiles from Figure 1 in KR99 which we intend to test when using real observations from PLATO. This involves expressing $\Omega^1_{\rm out}, \Omega^3_{\rm out}$ and $\Omega^1_{\rm in}$ in terms of $\bar{\Omega}_{\rm bot}, (\Omega_{\rm equator}-\Omega_{\rm pole})$ and Ω_0 (which parameters in KR99 as described below). The first thing to do is to select the rotation period $P_{\rm rot}$. Then, based on Figure 1 in KR99, we can determine the LDR $\frac{\Delta\Omega}{\Omega_0}$ from the left panel and the RDR $\left.\frac{\Delta\Omega}{\Omega_0}\right|_{\rm rad}$ from the right panel at that $P_{\rm rot}$. Because the rotation period is simply related to Ω_0 as $\Omega_0 = 2\pi/P_{\rm rot}$, we can then obtain $(\Omega_{\rm equator}-\Omega_{\rm pole})$ and $\bar{\Omega}_{\rm bot}$.

The definition of $\bar{\Omega}_{\rm bot}$ in Eqn. (B4) along with the parameterization of $\Omega(r,\theta)$ in Eqn. (B9) leads to the following equation:

$$\bar{\Omega}_{\rm bot} = \frac{3}{4}\int_0^\pi \Omega_1^{\rm in}\,\sin^3\theta\,{\rm d}\theta, \tag{B10}$$

where we have assumed that the rotation rate at the base of the convective envelope is represented by $\Omega_1^{\rm in}$. Note that we assume $F_{\rm in} = 1$ and $F_{\rm out} = 0$ at $r = r_{\rm cz}$ (assuming otherwise would mean $F_{\rm in} = 0$ and $F_{\rm out} = 1$ at $r = r_{\rm cz}$ in which case, the radial differential rotation would be zero). Evaluating the simple integral in Eqn. (B10) we find that

$$\bar{\Omega}_{\rm bot} = \Omega_1^{\rm in}, \tag{B11}$$

as $\int \sin^3\theta d\theta = 4/3$. Further, we note that $\Omega_{\rm equator} = \Omega(R,\pi/2)$ and that $\Omega_{\rm pole} = \Omega(R,0)$. Substituting these in Eqn. (B9) we get

$$\Omega_{\rm equator} - \Omega_{\rm pole} = -\frac{15}{2}\Omega_3^{\rm out}. \tag{B12}$$

Furthermore, by substituting the definition of Ω_0 from Eqn. (B3) in the parameterized form in Eqn. (B9) and subsequently computing the integration, we find that

$$\Omega_0 = \Omega_1^{\rm out}. \tag{B13}$$

Therefore, what we have is a one-to-one relation between the parameters in KR99 and those in our parameterization.

REFERENCES

Aerts, C., Mathis, S., & Rogers, T. M. 2019, ARA&A, 57, 35, doi: 10.1146/annurev-astro-091918-104359

Bellinger, E. P., Hekker, S., Angelou, G. C., Stokholm, A., & Basu, S. 2019, A&A, 622, A130, doi: 10.1051/0004-6361/201834461

Benomar, O., Goupil, M., Belkacem, K., et al. 2018, ApJ, 857, 119, doi: 10.3847/1538-4357/aab9b7

Borucki, W. J., Koch, D., Basri, G., et al. 2010, Science, 327, 977, doi: 10.1126/science.1185402

Brun, A. S., & Browning, M. K. 2017, Living Reviews in Solar Physics, 14, 4, doi: 10.1007/s41116-017-0007-8

Brussaard, P., & Tolhoek, H. 1957, Physica, 23, 955, doi: https://doi.org/10.1016/S0031-8914(57)95547-7

Chaplin, W. J., Elsworth, Y., Davies, G. R., et al. 2014, MNRAS, 445, 946, doi: 10.1093/mnras/stu1811

Chaplin, W. J., Houdek, G., Karoff, C., Elsworth, Y., & New, R. 2009, A&A, 500, L21, doi: 10.1051/0004-6361/200911952

Dahlen, F. A., & Tromp, J. 1998, Theoretical Global Seismology (Princeton University Press)

Deheuvels, S., García, R. A., Chaplin, W. J., et al. 2012, ApJ, 756, 19, doi: 10.1088/0004-637X/756/1/19

Edmonds, A. 1960, Angular Momentum in Quantum Mechanics, Investigations in physics (Princeton University Press). https://books.google.com/books?id=0vYNAQAAIAAJ

Gizon, L., Ballot, J., Michel, E., et al. 2013, Proceedings of the National Academy of Science, 110, 13267, doi: 10.1073/pnas.1303291110

Harvey, J. 1985, in ESA Special Publication, Vol. 235, Future Missions in Solar, Heliospheric & Space Plasma Physics, ed. E. Rolfe & B. Battrick, 199

Howe, R. 2008, Advances in Space Research, 41, 846, doi: 10.1016/j.asr.2006.12.033

Karak, B. B., Tomar, A., & Vashishth, V. 2020, MNRAS, 491, 3155, doi: 10.1093/mnras/stz3220

Kawaler, S. D., Sekii, T., & Gough, D. 1999, ApJ, 516, 349. https://arxiv.org/abs/astro-ph/9811286

Kitchatinov, L. L., & Rüdiger, G. 1999, A&A, 344, 911

Koch, D. G., Borucki, W. J., Basri, G., et al. 2010, ApJL, 713, L79, doi: 10.1088/2041-8205/713/2/L79

Libbrecht, K. G. 1992, ApJ, 387, 712, doi: 10.1086/171119

McQuillan, A., Mazeh, T., & Aigrain, S. 2014, ApJS, 211, 24, doi: 10.1088/0067-0049/211/2/24

Mestel, L. 1953, MNRAS, 113, 716, doi: 10.1093/mnras/113.6.716

Montalto, M., Piotto, G., Marrese, P. M., et al. 2021, arXiv e-prints, arXiv:2108.13712. https://arxiv.org/abs/2108.13712

Nielsen, M. B., Gizon, L., Schunker, H., & Schou, J. 2014, A&A, 568, L12, doi: 10.1051/0004-6361/201424525

Nielsen, M. B., Schunker, H., Gizon, L., Schou, J., & Ball, W. H. 2017, A&A, 603, A6, doi: 10.1051/0004-6361/201730896

Potter, A. T., Tout, C. A., & Eldridge, J. J. 2012, MNRAS, 419, 748, doi: 10.1111/j.1365-2966.2011.19737.x

Ritzwoller, M. H., & Lavely, E. M. 1991, ApJ, 369, 557, doi: 10.1086/169785

Ruediger, G. 1989, Differential rotation and stellar convection. Sun and the solar stars

Schou, J., Antia, H. M., Basu, S., et al. 1998, ApJ, 505, 390, doi: 10.1086/306146

Schunker, H., Schou, J., Ball, W. H., Nielsen, M. B., & Gizon, L. 2016, A&A, 586, A79, doi: 10.1051/0004-6361/201527485

Spruit, H. C. 2002, A&A, 381, 923, doi: 10.1051/0004-6361:20011465

Stahn, T. 2010, Analysis of time series of solar-like oscillations - Applications to the Sun and HD52265, Fakultät für Physik (inkl. GAUSS). https://ediss.uni-goettingen.de/handle/11858/00-1735-0000-0006-B52E-5?locale-attribute=en

Suto, Y., Kamiaka, S., & Benomar, O. 2019, AJ, 157, 172, doi: 10.3847/1538-3881/ab0f33

Vorontsov, S. V. 2011, Monthly Notices of the Royal Astronomical Society, 418, 1146, doi: 10.1111/j.1365-2966.2011.19564.x

Zahn, J. P. 2008, Communications in Asteroseismology, 157, 196